PAPER • OPEN ACCESS

Near-null interferometric test of aspheric cylinders utilizing a partial null lens

View the article online for updates and enhancements.

Near-null interferometric test of aspheric cylinders utilizing a partial null lens

Shuai Xue[1,2,3,4,*] ⦿**, Lingwei Kong**[1,2,3]**, Yifan Dai**[1,2,3]**, Shanyong Chen**[1,2,3] **and Zhifan Lin**[1,2,3]

[1] College of Intelligent Science, National University of Defense Technology, Changsha, Hunan 410073, People's Republic of China
[2] Hunan Key Laboratory of Ultra-Precision Machining Technology, Changsha, Hunan 410073, People's Republic of China
[3] Laboratory of Science and Technology on Integrated Logistics Support, National University of Defense Technology, Changsha, Hunan 410073, People's Republic of China
[4] State Key Laboratory of Digital Manufacturing Equipment and Technology, Wuhan, Hubei 430000, People's Republic of China

E-mail: shuaixue1990@163.com

CrossMark

Abstract

Aspheric cylinders are more advantageous than cylinder with spherical cross section in optical design and aberration correction of high-energy laser systems because additional shape parameters can be introduced. To overcome the limited test accuracy and the insufficient research on the testability of the flexible null test method for aspheric cylinders, a near-null interferometric test method for aspheric cylinders was developed utilizing a partial null lens. A coaxial configuration design was employed. Accordingly, only one translation motion was required for testing various aspheric cylinders in one shot. Using the proposed test configuration and the developed near-null data processing method, test accuracy about $\lambda/20$ ($\lambda = 632.8$ nm) root-mean-square are easier to guarantee compared with those of the existing stitching-required method with off-axis configuration. Further, the testability of the proposed method was analyzed following the development of the partial null theory. The analysis shows the testable surfaces are equidistant surfaces with nearly constant $k \cdot R$ products ($k \cdot R = 211.625$ mm). The testability results can serve as a good reference for engineers who intend to use aspheric cylinders in high-energy laser systems and can further promote the development of high-energy laser systems. A near-null test system was established. Its simple configuration, moderate test accuracy, and flexible test capacity were successfully demonstrated based on aspheric cylinders measurements.

Keywords: interferometric surface figure test, high-energy laser, aspheric cylinders, non-null test

(Some figures may appear in colour only in the online journal)

1. Introduction

Cylindrical optics are generated by the parallel translation of a straight line along a curve. Owing to the different focal powers of the meridional and sagittal planes, cylindrical optics are extensively utilized to correct astigmatism in laser resonators [1, 2] and beam shaping units [3] in high-energy laser systems. Similar to the terms of spherical surfaces and aspheric surfaces, cylinder with aspheric cross section can be termed as aspheric cylinders. The term 'acylindrical surfaces' should never be used: The prefix 'a' (latin origin) means 'non', therefore making from a 'spheric' an 'aspheric', i.e. a 'non-spheric' surface. That makes sense. The word 'acylindrical' means 'non-cylindrical', which is nonsense. Aspheric cylinders are more advantageous than cylinder with spherical cross section

---

for optical design and aberration correction because additional shape parameters can be introduced. Aspheric cylinders are increasingly preferred by engineers who design and construct high-energy laser systems to achieve better performance in terms of higher energy, better focusing, and compact structure. The typical desired surface figure accuracy of aspheric cylinders in high-energy laser systems is better (smaller) than 0.1 μm peak-to-valley (PV). With the development of fabrication techniques for aspheric cylinders, such as the slow tool servo diamond turning process [4] and magnetorheological finishing [5], it is envisaged that aspheric cylinders will be widely used in high-energy laser systems. To guide the iterative fabrication process, surface figure test of the aspheric cylinders is required. As the most commonly used high-accuracy testing method, interferometric testing of cylindrical surfaces requires a customized computer-generated hologram (CGH) [6, 7] to transform standard flat or spherical wavefronts into wavefronts with the same shape as that of the test surface. The CGH test method for cylindrical surfaces can adaptive for testing cylindrical surfaces with different radius of curvature (ROC) and aperture [8–14] because the shape of cylindrical wavefront is also cylindrical wavefront after transmitted for a distance. However, CGH is unique to a single specific aspheric cylinder. Moreover, CGH is expensive and has a long lead time. Hence, the CGH null method is cost-prohibitive for various aspheric cylinders. Developing a flexible interferometric test method for testing various aspheric cylinders is important for the enhancement of the test efficiency and reduction of cost.

Peng *et al* conducted excellent and pioneering work on breaking down the static test mode for interferometric tests of aspheric cylinders [15]. By yawing the cylinder null (designed for a circular cylindrical surface) at different angles, variable wavefronts can be generated to compensate for most of the aberrations for different off-axis subapertures of the aspheric cylinder. After stitching the test results of the subapertures, the full aperture of the aspheric cylinder can be acquired. Peng *et al* successfully tested an aspheric cylinder with a departure of up to 81 μm from the best-fitting circular cylinder with the use of the reported method. The test accuracy was verified by a contact three-dimensional (3D) profilometer (Talysurf PGI Freeform). However, the nominal test accuracy of Talysurf PGI Freeform is only ±0.15 μm. Further, the PV value difference between the test result of the yawing CGH method with that of the Talysurf PGI Freeform method is 0.159 μm. Moreover, the phase distribution of the two test results is not quantitively compared. Therefore, the measurement accuracy of the yawing CGH method is not clearly identified.

Research on flexible tests for aspheric cylinders has been scarce. However, many studies have focused on flexible null tests for aspheric surfaces. The basic idea of using a null to test various aspheric surfaces is to violate the null condition and use non-null configurations. Null fringes are not required, and the surface is testable if the deviation between the test wavefront and the test surface is within the dynamic range of the interferometer. Liu and Hao *et al* used a doublet as a partial null to conduct a non-null test for aspheric concave surfaces. The adaptable departure for aspheric surfaces is in the range of

92.8–121.7λ (λ = 632.8 nm) [16, 17]. Yang *et al* [18, 19] and Greivenkamp *et al* [20, 21] used a singlet collimated for partial null tests of aspheric surfaces. Because of the violation of the null condition, rays from the test and reference arms will not follow the same path, and the surface figure error of the test surface can be coupled with the retrace error. Yang *et al*, Liu *et al*, Tian *et al*, He *et al*, Shi *et al*, and Zhang *et al* developed a retrace error calibration method to determine the useful surface figure error from the test results [18–25].

Compared with the mature flexible null test method for aspheric surfaces, the current flexible null test method for aspheric cylinders is difficult to guarantee the test accuracy within ~λ/20 root-mean-square (RMS). The current flexible null test method for aspheric cylinders is complex in terms of optical configuration; the optical system has an off-axis configuration, and the aspheric cylinders can only be measured by stitching. The off-axis configuration and stitching test scheme make it difficult to align the test surface and the CGH in the non-null test. Stitching is required to obtain the full aperture figure error, which further complicates the test system and decreases the test accuracy. Furthermore, the current method for flexible tests of aspheric cylinders does not explain why the test system can generate variable aberrations. The measurable range of aspheric cylinders has not been clearly identified. The relations among the testable surfaces were also not expounded. Engineers who design and construct high-energy systems may hesitate to adopt an aspheric cylinder that can be tested by the flexible test method rather than spending more time and money to design and manufacture a specific CGH for testing. The insufficient research on the testability of the flexible null test method for aspheric cylinders hinders the application of aspheric cylinders in high-energy laser systems. Briefly, developing a flexible null test method with an accuracy about λ/20 RMS, whereby the test can be performed in one shot rather than by stitching, in coaxial configuration rather than in off-axis configuration, and thorough analyses of the testability remain challenging.

To this end, we propose a near-null interferometric test method for aspheric cylinders utilize a partial null lens. To achieve test accuracy of ~λ/20 RMS, a simple test configuration and the near-null data processing method is developed. The proposed flexible null test is achieved by moving the aspheric cylinders back and forth relative to a cylindrical partial null lens. At the best fitting position, the cylindrical partial null lens can partially null the aberration of the aspheric cylinder. The test configuration was coaxial, and the aspheric cylinders could be tested by a single shot rather than by stitching. The alignment of the proposed test system and the test accuracy are easier to guarantee compared with those of the existing off-axis configuration and stitching method. Furthermore, near-null data processing method to recover the surface figure error of the test aspheric cylinder from the near-null test result with high accuracy was developed. To evaluate the testability of the proposed method, theoretical analysis was conducted. The results of the theoretical analysis indicate that the testable surfaces are equidistant surfaces with nearly constant $k \cdot R$ products ($k \cdot R = 211.625$ mm), where k is the conic constant and R is the ROC. The testable aspheric cylinders

have nearly constant one-dimensional spherical aberrations. A concave aspheric cylinder with $R = 200$ mm, $k = -1$ and an aperture of 85×52 mm^2 (arc direction $\times$ linear direction) was tested to validate the feasibility of the proposed method. The test accuracy is $\sim\lambda/20$ RMS, as verified by the stigmatic null test method and evaluated by the structural similarity index (SSIM index). The proposed method can help enhance the test efficiency for aspheric cylinders. The test accuracy verification and testability analyses can serve as a reference for engineers who intend to use aspheric cylinders in high-energy laser systems, and promote the application of aspheric cylinders in high-energy laser systems.

The remainder of this paper is organized as follows. Section 2 presents the test principles of the proposed method. A theoretical analysis of the testability of the proposed method is then presented. Section 3 describes the experimental validation, and the discussion is presented in section 4. Finally, the paper is concluded in section 5.

2. Material and methods

The basic principle of the near-null test method for aspheric cylinders, which utilizes a partial null lens, is shown in figure 1. The collimated beam from the interferometer is converted to a wavefront by a partial null lens. For demonstration purposes, a plano-convex cylindrical lens was used. The wavefront is not required to have the same shape as the nominal test surface; however, the departure of the wavefront from the nominal test surface must be within the dynamic range of the interferometer. The distance from the flat surface of the near-null to the test surface was optimized to meet the near-null condition. The distance from the flat surface of the near-null to the test surface was maintained through low-coherence interferometry. The test beam was then converted to a nearly collimated beam after it was reflected from the test surface. The nearly collimated beam comprises the surface figure of the test surface, the departure of the wavefront from the nominal test surface, the retrace error due to the near-null test, and misalignment aberration. Notably, owing to the deviation from the null configuration, rays from the test and reference arms do not follow the same path, and retrace errors exist. The nearly collimated beam interferes with the reference beam within the interferometer, and an interferogram that can be resolved by the charge-coupled device (CCD) of the interferometer is generated. The wavefront error can be acquired after phase shifting and unwrapping. The surface figure of the test surface can be reconstructed from the wavefront error test result after data processing of the near-null test for aspheric cylinders. The two key points of the partial null test for aspheric cylinders involve partial null theory for aspheric cylinders and data processing of near-null tests for aspheric cylinders.

2.1. Partial null theory for aspheric cylinders

The partial null theory for aspheric cylinders reveals the relations between the partial null parameters and testable surface parameters, and the test ability of a certain partial null. To establish the partial null theory, the paraxial aberration balance of the partial null configuration shown in figure 1 was analyzed as follows.

An aspheric cylinder (equation (1)) was considered

$$z = \frac{cy^2}{1 + \sqrt{1 - (k+1)c^2 y^2}} + \sum_{i=1}^{N} \alpha_i y^{2i}, \tag{1}$$

where z denotes the surface sag, y denotes the lateral coordinate along the y-axis, k represents the conic constant, c represents the vertex curvature, N denotes the number of high-order aberration terms, and α_i denotes the coefficients of high-order aberrations. The dominant aberration of the aspheric cylinder compared with the corresponding best-fit cylindrical surface is one-dimensional primary spherical aberration (1D-PSA). The basic idea of a near-null test for aspheric cylinders is to balance the majority of the 1D-PSA of the test surface using a null. In the paraxial region, the coefficient of 1D-PSA for an aspheric cylinder can be expressed as [26–28]:

$$S_{\mathrm{I}}^{(\mathrm{t})} = 2kRu^4, \tag{2}$$

where $S_{\mathrm{I}}^{(\mathrm{t})}$ denotes the coefficient of 1D-PSA, R represents the vertex ROC, and u represents half of the aperture angle.

Based on the Seidel aberration theory [26–28], the coefficient of 1D-PSA for a thin lens located in a collimated beam can be expressed as

$$S_{\mathrm{I}}^{(\mathrm{n})} = \left[\frac{n+2}{n} \frac{1}{r_1^2} \varphi - \frac{2n+1}{n-1} \frac{1}{r_1} \varphi^2 + \frac{n^2}{(n-1)^2} \varphi^3 \right] h^4, \tag{3}$$

where h denotes the aperture height of the thin lens, r_1 and is the Roc of the left surface of the thin lens, n denotes the refractive index, and φ is the power of the thin lens. For the thin lens,

$$\varphi = (n-1)(1/r_1 - 1/r_2), \tag{4}$$

where r_2 is the Roc of the right surface of the thin lens. For a plano-convex lens with a convex surface facing the interferometer,

$$r_2 = \infty. \tag{5}$$

In the paraxial region, $u = \tan u$. Therefore,

$$h = fu, \tag{6}$$

where f denotes the focal length, as shown in figure 1. Moreover, f and φ adhere to the following equation

$$\varphi = 1/f. \tag{7}$$

Substitution of equations (4)–(7) into equation (3) yields

$$S_{\mathrm{I}}^{(\mathrm{n})} = Pfu^4, \tag{8}$$

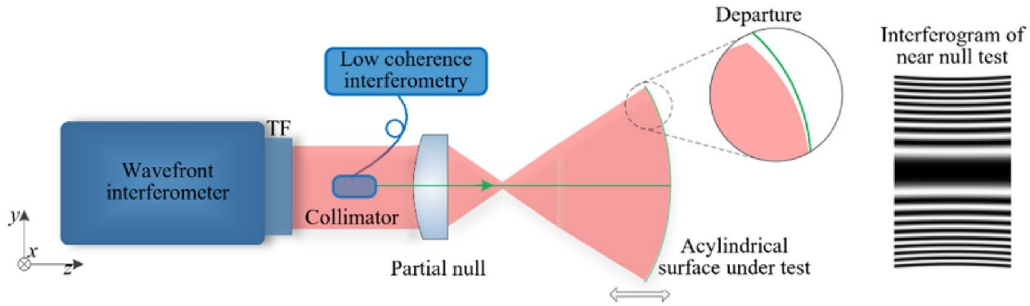where

$$P = \frac{n^2(n-2) + 2}{n(n-1)^2}, \tag{9}$$

Figure 1. Optical layout of the near-null test for aspheric cylinders.

and

$$f = \frac{r_1}{(n-1)}. \tag{10}$$

The near-null test means that the 1D-PSAs of the thin lens and the test surface should be balanced, that is,

$$S_I^{(t)} + 2S_I^{(n)} = 0. \tag{11}$$

Substitution of equations (2) and (8) into equation (11) yields

$$kR = -Pf. \tag{12}$$

Equation (10) shows that for a certain null lens with parameters f and P, a range of aspheric cylinders with parameters k and R such that $kR = -Pf$ can be tested in the paraxial sense. The testable aspheric cylinders had an appropriate constant coefficient for 1D-PSA. Furthermore, these testable aspheric cylinders are equidistant.

The partial null testing theory for aspheric cylinders can also be interpreted from the viewpoint of wavefront propagation. Suppose a wavefront W_1 with shape parameters k_0 and R_0. The shape parameters k_t and R_t of wavefront W_2, which is the wavefront in which W_1 propagates forward with a minor distance t satisfy the relation [29]

$$k_t R_t = k_0 R_0. \tag{13}$$

Equation (13) implies that if an aspheric cylinder with the shape parameters k_0 and R_0 can be tested by wavefront W_1, another aspheric cylinder with shape parameters k_t and R_{0+t} can be tested by W_2.

Based on the theoretical analysis presented above, it can be summarized preliminarily that a partial null can adapt to a range of aspheric cylinders in the sense of paraxial theory. Furthermore, the testable aspheric cylinders are equidistant surfaces with constant shape parameters kR and an appropriate 1D-PSA constant coefficient $S_I^{(t)}$. Moreover, the shape constant of the testable surfaces is determined by the shape parameters of the partial null lens, that is, $kR = -Pf$.

Simulations were conducted to verify the above theoretical analysis with the use of a typical concave aspheric cylinder as the test surface with $k = -1$ and $R = 200$ mm. The clear aperture was $D_a \times D_l = 85 \times 52$ mm^2 (arc direction $\times$ linear direction). Figure 2 shows the departure of the test surface from its best-fitted cylindrical surface
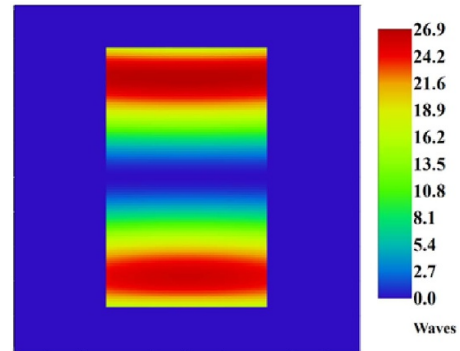

Figure 2. Deviation of the test surface from its best fitted cylindrical surface.

(Roc = 202.675 mm) is mainly 1D-PSA with a PV of 26.941λ ($\lambda = 632.8$ nm). By substituting $n \approx 1.516$ (refractive index of K9 glass), $k = -1$, and $R = 200$ mm in equations (9), (10) and (12), the initial shape parameters of the partial null can be obtained as $r_1 = 46.929$ mm. The aperture of the partial null can be obtained as $D = D_a/R \times f = 38.653$ mm. After searching for the stocks of the lens supplier, the parameters of the partial null are determined as $r_1 = 54.274$ mm, $D_{an} \times D_{ln} = 52 \times 52$ mm^2 (arc direction $\times$ linear direction), and center thickness $T = 18.5$ mm. A test scheme using the above partial null for testing the test surface was then established using the optical design software. A schematic of the optical model of the test system is shown in figure 3. Optimization was conducted to meet the near-null condition. The optimization variable is the distance l from the vertex of the test surface to the flat surface of the partial null. The optimization goal involved the minimization of RMS value of the residual wavefront error. After the optimization was completed, $l = 293.032$ mm. Figure 4 shows the residual aberration with PV = 1.1929λ and RMS = 0.3869λ. The maximum slope of the residual aberration is within the dynamic range of a typical interferometer equipped with a CCD of 1000 pixels $\times$ 1000 pixels resolution. Notably, the dynamic range indicates the maximum frequency of the interference fringes, which is equal to the Nyquist frequency of the CCD. The nominal interferogram fringes are shown in figure 5. These fringes can be resolved using a common interferometer. Simulations were conducted to verify that the partial null can test a series of equidistant aspheric cylinders, and these surfaces were found
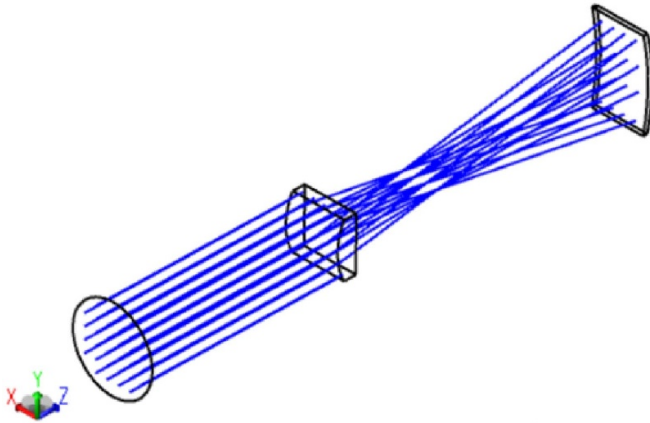
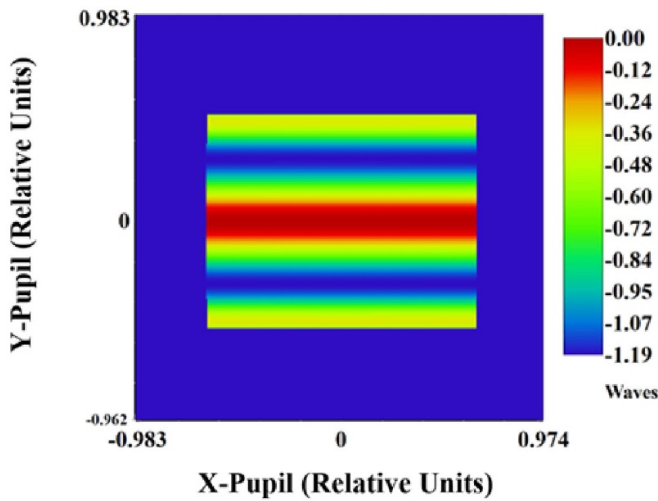**Figure 3.** Optical model of the test system.

Figure 4. Residual aberration.

Figure 5. Nominal interferogram fringes.

retrace error due to the near-null test, and the misalignment aberration, that is,

$$W_n = f(W_t, W_d, W_r, W_m), \tag{14}$$

where W_n denotes the near-null test result, W_t denotes the surface figure error of the test surface, W_d denotes the theoretical departure of the test surface, W_r denotes the retrace error, W_m denotes the misalignment aberration, and f represents the relationship between (W_t, W_d, W_r, W_m) and W_n. The function f is determined by the wavefronts/aberrations in the optical system and the configuration of the optical system. For a flat wavefront that transmits in a flat optical window system, the analytical form of f is straightforward. However, complex wavefronts (i.e. wavefronts that are not flat or spherical) do not propagate linearly in complex optical systems; therefore, the analytical form of f is nonlinear and is difficult to establish.

Two methods can be used for mitigating this issue. The first method is the optimization based on modeling. First, the optical model of the test system, as presented in figure 3, is established. Legendre polynomials [29] are commonly used to characterize the wavefronts and surfaces. The first ten terms of the Legendre polynomials are listed in table 1 and are shown in figure 7. Furthermore, Legendre polynomials are orthogonal in the rectangular region, which is the typical aperture shape of aspheric cylinders. Therefore, W_n and W_t are represented as the Legendre phase in the model, that is,

$$W_n = \sum_{i=1}^{N} A_i L_i, \tag{15}$$

$$W_t = \sum_{i=1}^{M} B_i L_i. \tag{16}$$

where L_i denotes the ith Legendre polynomial. N and M denote the number of Legendre coefficients in the series for W_n and W_t, respectively. A_i and B_i represent the coefficients of the ith Legendre polynomial for W_n and W_t, respectively. Notably, the Legendre phase does not correspond to a common

to have nearly constant shape parameters kR. During the simulations, the distance from the test surface to the paraxial focus of the partial null lens l' was varied from 50 mm to 1000 mm with increments of 1 mm. For each l' value, optimization was conducted to determine the testable aspheric cylinder. The optimization variables are k and R of the test surface. The optimization goal is to minimize the RMS value of the residual wavefront error. The testability criterion is that the maximum slope of the residual aberration is within the dynamic range of a typical interferometer equipped with a CCD with a resolution of 1000×1000 pixels. The $k \cdot R$, k, and R values of the testable surface with l' are presented in figure 6. The mean and variance of the $k \cdot R$ values were 211.625 mm and 1.038 mm, respectively. The testable surfaces had an approximately constant $k \cdot R$ value.

2.2. Data processing of near-null test for aspheric cylinders

Near-null data processing comprises coordinates mapping and phase correction. Phase correction should first be conducted. The surface figure of the test surface is coupled with the departure of the test wavefront from the nominal test surface, the
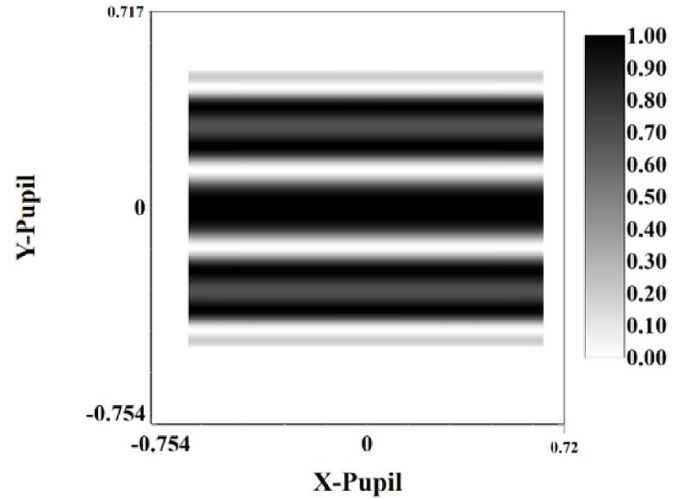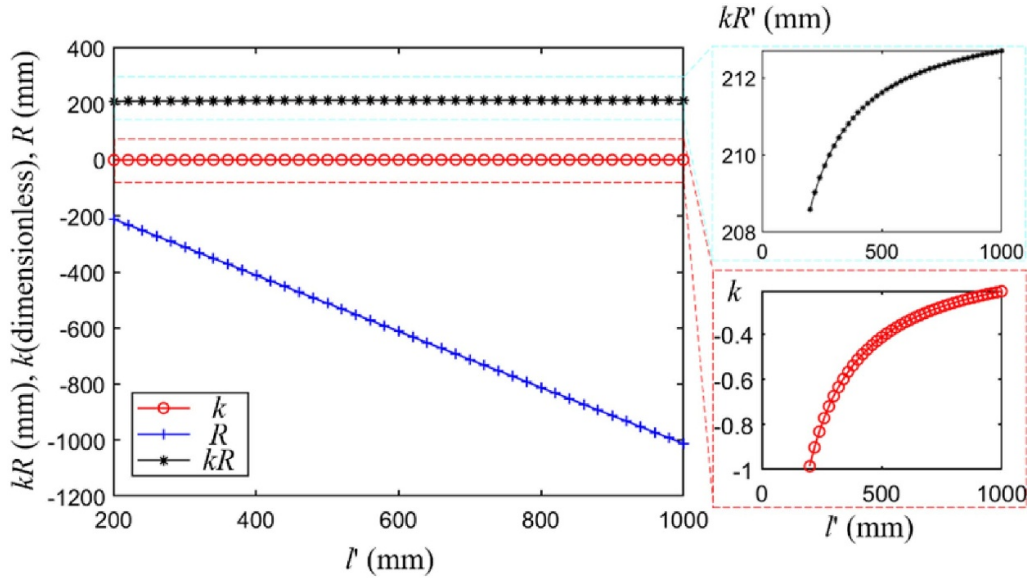
Figure 6. $K·R$, k, and R values of the testable surface as a function of l'.

Table 1. Definitions of Legendre polynomials.

Order	Aberration name	Polynomials
Q_1	Piston	1
Q_2	x-tilt	$\sqrt{3}x$
Q_3	y-tilt	$\sqrt{3}y$
Q_4	x-power	$\sqrt{5}/2(3x^2-1)$
Q_5	Astigmatism	$3xy$
Q_6	y-power	$\sqrt{5}/2(3y^2-1)$
Q_7	$0°$ coma	$\sqrt{7}/2(5x^3-3x)$
Q_8	$90°$ trefoil	$\sqrt{15}/2(3x^2-1)y$
Q_9	$0°$ trefoil	$\sqrt{15}/2(3y^2-1)x$
Q_{10}	$90°$ coma	$\sqrt{7}/2(5y^3-3y)$

surface in optical design software, and a user-defined surface is required.

The misalignment aberrations for testing the aspheric cylinders are those of the piston, x-tilt, y-tilt, y-power, and twist [30, 31], which are introduced by six degree-of-freedom misalignment of the test surfaces, that is,

$$W_m = a + bx + cy + dy^2 + exy = g_t(t_x, t_y, t_z, d_x, d_y, d_z). \quad (17)$$

where *a*, *b*, *c*, *d*, and *e* denote the coefficients of the piston, x-tilt, y-tilt, y-power, and twist, respectively. t_x, t_y, t_z, d_x, d_y, and d_z denote the tilt around the x-, y-, and z-axes, and the translation along the x-, y-, and z-axes, respectively. $g_t(·)$ denotes the posture and position of the test surface in the model of the test system. W_d and W_r can be automatically generated after W_m and W_t are determined in the model. Optimizations were conducted to obtain W_t from W_n. The optimization variables were B_1, B_2, …, B_M, t_x, t_y, y_z, d_x, d_y, and d_z. The optimization goal involved the setting of the Legendre coefficients of the wavefront received on the image plane to A_1, A_2, …, A_N. W_t can be obtained using equation (16) after the optimization was
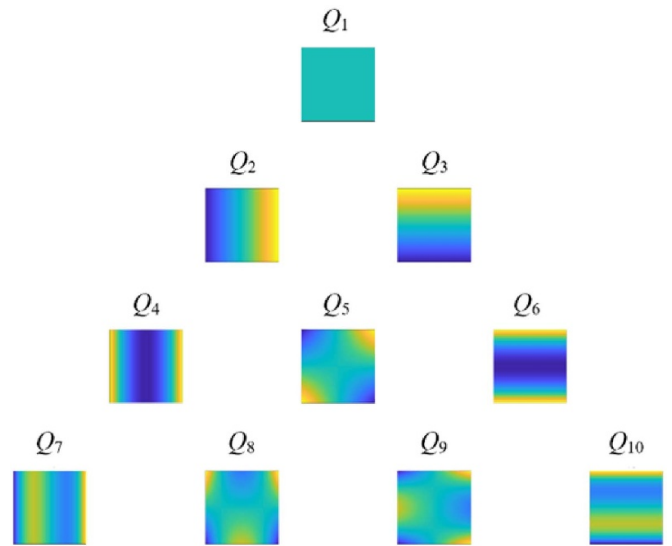

Figure 7. Maps of Legendre polynomials.

completed. The method considered the propagation effects of W_t, W_d, W_r, and W_m; hence, it can be used in situations in which the surface figure error and/or theoretical residual wavefront are relatively large [25].

When W_t is relatively small and the theoretical residual wavefront is moderate, a simpler method can be adopted to recover W_t. Equation (14) can be simplified as

$$W_n = W_t + g(W_d, W_r) + W_m, \quad (18)$$

where $g(W_d, W_r)$ is the residual aberration of the theoretical test system, that is, the wavefront on the image plane of the theoretical test system. W_t can be obtained by subtracting the residual aberration and best-fitted misalignment aberrations from the near-null test result, that is,

$$W_t = W_n - g(W_d, W_r) - a + bx + cy + dy^2 + exy, \quad (19)$$

where *a*, *b*, *c*, *d*, and *e* are obtained by fitting $W_n - g(W_d, W_r)$ with polynomials $a + bx + cy + dy^2 + exy$.

After phase correction is completed, mapping correction [32, 33] should be conducted. The acquired near-null test data were presented in the imaging coordinate frame. The pixel coordinates are transformed into the workpiece coordinate frame. Aspheric cylinders have different curvatures along the linear and arc directions. Thus a nonlinear mapping relationship is established between the pixel coordinates (u, v) and the workpiece transverse coordinates (x_0, y_0). Furthermore, rays from the test and reference arms do not follow the same path, which exacerbates the nonlinear mapping effect. We denote the mapping function between (u, v) and (x_0, y_0) as *h*

$$(x_0, y_0) = h(u, v). \quad (20)$$

To obtain *h*, a bundle of rays was traced from the imaging plane to the test surface. Ray tracing was conducted based on macro programming with the use of the optical design software. The ray-tracing results presented in the form of four columns of data (u, v, x_0, y_0) serve as a numerical form of *h*. Coordinates (x_0, y_0) on the test surface of any ray with transverse coordinates (u, v) on the imaging plane can be determined via interpolation.

Simulations were conducted to verify the proposed data processing method for the near-null test of aspheric cylinders. The test surface and partial null are the same as those described in section 2.1. Furthermore, the theoretical test system is the same as that shown in figure 3. A practical test system was established to simulate the practical test result W_n. The practical test system in the simulation is similar to that shown in figure 3, but the differences are that the surface figure error is added up to the test surface and the posture of the test surface deviates from its nominal posture. In the simulation of the practical test system, the surface type of the test surface is a biconic Zernike and is defined as [34]

$$z = \frac{c_x y^2 + c_y y^2}{1 + \sqrt{1 - (k_x + 1)c_x^2 x^2 - (k_y + 1)c_y^2 y^2}} + \sum_{i=1}^{16} \alpha_i x^i + \sum_{i=1}^{16} \beta_i y^i + \sum_{i=1}^{N} C_i Z_i(\rho, \varphi), \quad (21)$$

where c_x and c_y are the vertex curvatures along the *x*-and *y*-axes, respectively, k_x and k_y are conic constants along the *x*-and *y*-axes, respectively, and Z_i are the Zernike terms [35]. *N* denotes the number of Zernike coefficients in the series, C_i represents the coefficient of the ith Zernike standard term, ρ denotes the normalized radial ray coordinate, and φ denotes the angular ray coordinate. Coefficient C_i has units of mm. The Zernike term was used to simulate the surface figure error of the test surface. For the test surface, $c_y = 1/200$ mm^{-1}, $k_y = -1$, $c_x = k_x = 0$, $Z_7 = 1e - 4$ mm, $Z_8 = 1e - 4$ mm. The normalization radius for the Zernike terms was set to 55 mm. The misalignments of the test surface are $t_x = 0.001°$,

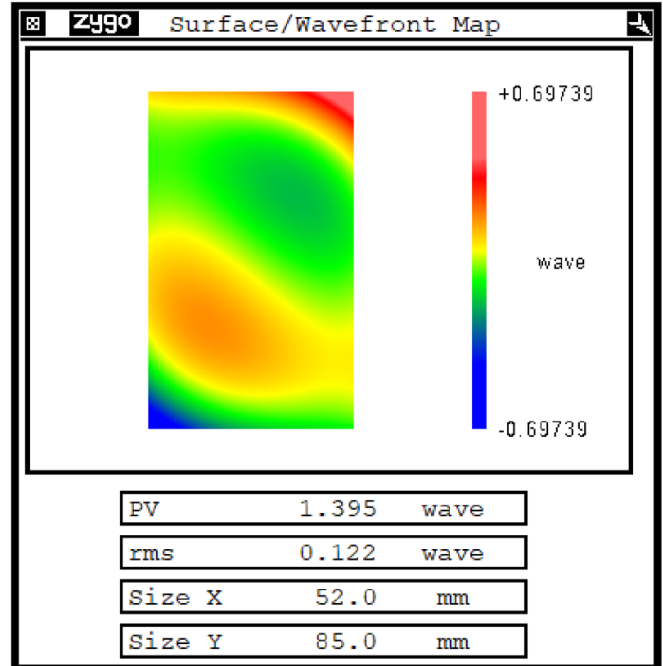**Figure 8.** Theoretical surface error of the test surface.

$t_y = 0.001°$, $t_z = 0.005°$, $d_z = 0.001$ mm. The theoretical surface error (along the normal direction) of the test surface is shown in figure 8 with an RMS 0.122λ. The near-null test results obtained from the simulated practical test system are shown in figure 9 with an RMS of 0.335λ. Evidently, the phase distribution and transverse coordinate mapping of the surface figure severely deviate from the theoretical surface figure shown in figure 2. To reconstruct the surface figure error from the near-null test result, as shown in figure 9, phase correction and mapping correction were conducted. The residual aberration of the theoretical test system shown in figure 2 is first subtracted from the test result to separate the deviation of the test surface and the retrace error. The results are presented in figure 10. Notably, the misalignment aberrations were coupled. The piston, *x*-tilt, *y*-tilt, *y*-power, and twist terms are fitted and subtracted from the surface height map shown in figure 10. The surface height map obtained after the phase correction is shown in figure 11. As shown in figure 11, the surface height map is in the CCD frame. To transform the pixel coordinates into the workpiece coordinate frame, an array (1024×1024) of rays is traced from the imaging plane to the test surface. The footprints of the rays on the imaging plane and on the test surface are shown in figure 12. The transverse coordinates (x_0, y_0) on the test surface corresponding to the pixel coordinates of the surface height map shown in figure 11 can be determined via interpolation using ray tracing data. The recovered surface figure after the phase and mapping corrections is shown in figure 13 with an RMS of 0.126λ. The phase distribution and the PV and RMS values were very similar to those of the theoretical surface figure error. The point-to-point difference between the recovered surface figure and the theoretical surface figure is shown in figure 14 with RMS = 0.006λ.
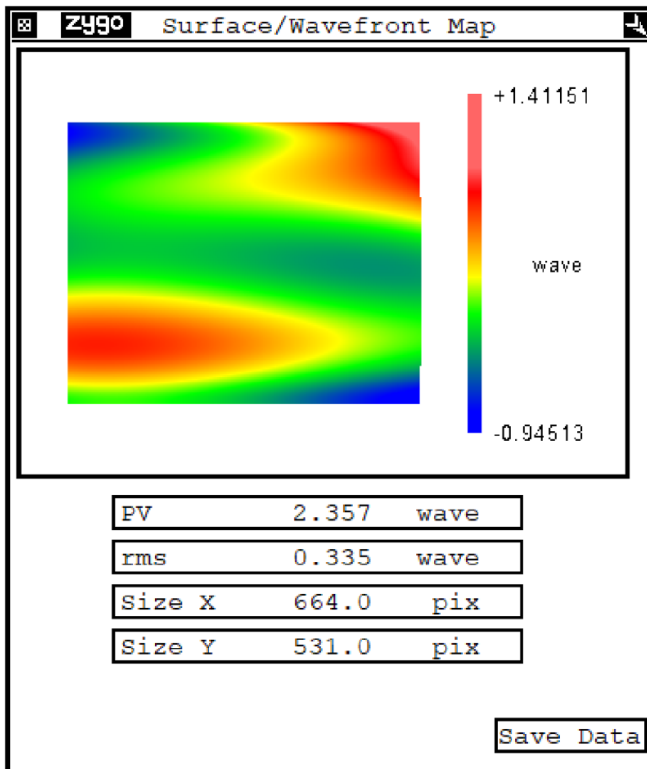
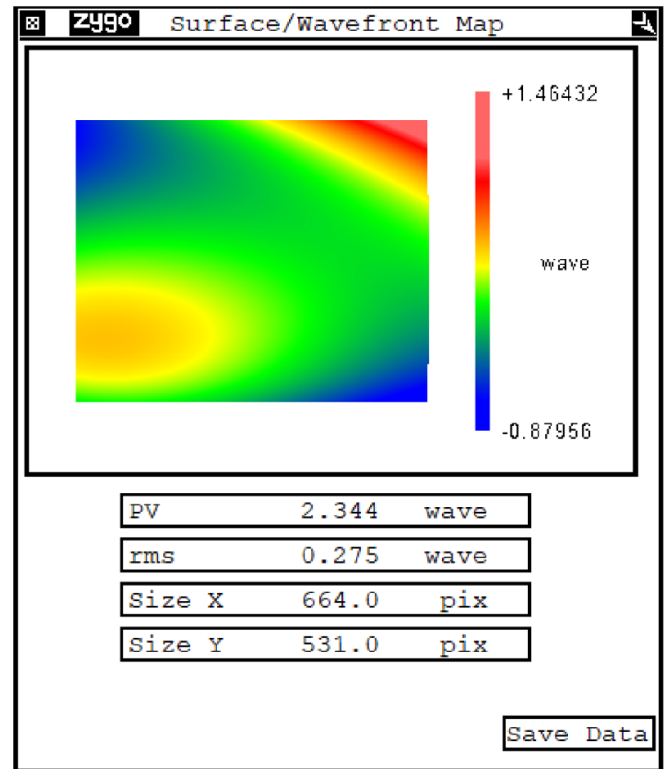**Figure 9.** Near-null test result obtained from the simulated practical test system.

Figure 10. Results associated with the subtraction of residual aberration of the theoretical test system from the near-null test result.

2.3. Error analyses

The error sources of the partial null test method mainly include misalignment error, imperfect manufacturing error, and retrace error calibration. These are analyzed as follows.

Misalignment error include misalignment of the partial null and the test surface. As for the partial null, misalignment degrees of freedoms (dofs) are tilt. The tilt of the partial null can be adjusted by nulling the fringes of the interferogram formed by the reflected beams from the center region of the cylindrical surface of the partial null (can be regarded as a small flat) and the flat surface of the partial null. Simulations show that, to control the misalignment-induced aberrations within 0.01λ RMS (the test surface and partial null are the same as those described in section 2.1), mean tolerance requirement on tilt of the partial null is about $\pm 50''$. This can be easily accomplished by nulling the fringes.

As for the test surface, misalignment dofs are tilt around the *x*-, *y*-, and *z*-axes, and the translation along the *y*-, and *z*-axes. The distance between the partial null and the test surface is monitored by a distance measuring set LenScan LS600. LenScan LS600 can measure center thickness of optical elements and air gaps along the optical axis based on low coherence interferometry. Its measurement range is 600 mm with absolute accuracy of ± 1 μm. Simulation shows the misalignment aberration is smaller than 0.01λ RMS if the distance error is ± 1 μm. As shown in table 2, the misalignment aberration introduced by t_x (and d_y), t_y, t_z, and d_z are tilt-*y*, tilt-*x*, twist, and power-*y*, respectively [36]. As these aberrations can be subtracted according to equation (19), the

error introduced the misalignment is determined by the performance of the misalignment removal method. This has been investigated in [30]. For a test surface with *F*/1.5, 45 mm aperture and 69 mm Roc, the residual errors after subtracting the misalignment aberration induced by $t_y = 0.001°$, $t_z = 0.01°$, $d_y = 0.001$ mm, $d_z = 0.01$ mm are smaller than 0.0058λ RMS. When the tested surface is seriously misaligned or has a fast F/# or has a large surface figure error, high-order misalignment aberrations compensation method can be used for achieving higher accuracy [31]. The detailed error analysis on the misalignment aberration removal method can be referred to [30] and [31]. Therefore, using the nulling fringes method (for tilt of the partial null), low coherence interferometry (for d_z of the test surface), and the misalignment aberrations removal method (for t_x, d_y, t_y, t_z, and d_z of the test surface), the influences of alignment errors can be controlled within 0.01λ RMS.

Imperfect manufacturing error include the surface shape and glass homogeneity errors of the partial null lens. The surface figure error of the cylindrical surface of the partial null is tested by a Zygo interferometer with a CGH. The test result is about 0.03λ RMS. Because the test beam refracts at this surface, its contribution to test result is about $(n-1)\cdot 0.03\lambda \approx 0.015\lambda$ RMS, where *n* is the refractive index $n \approx 1.516$. The surface figure error of the flat surface of the partial null is about 0.008λ RMS. Similarly, its contributions to test result is about 0.004λ RMS.

For glass with homogeneity quality $\Delta n = 0.2 \times 10^{-6}$, its contribution to test result is about $\Delta W = \Delta n \times L = 0.2 \times 10^{-6}$
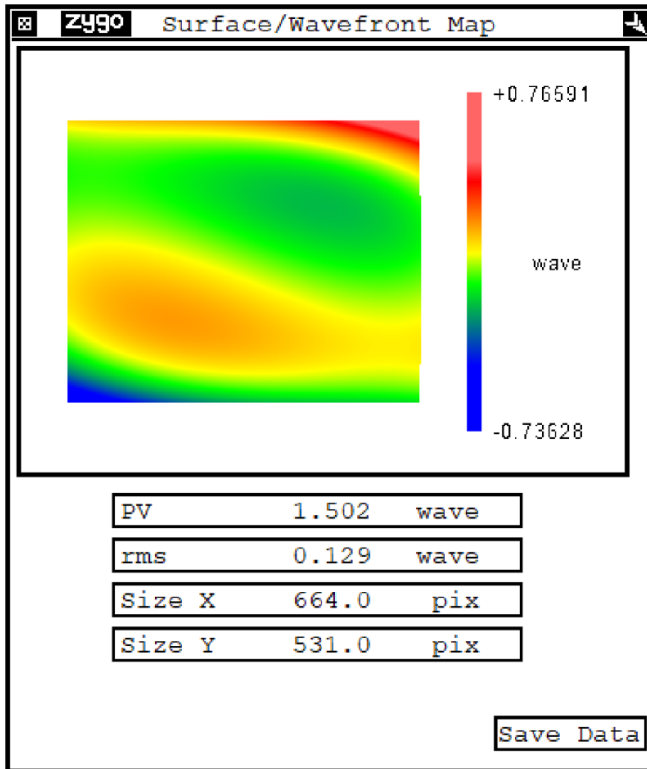
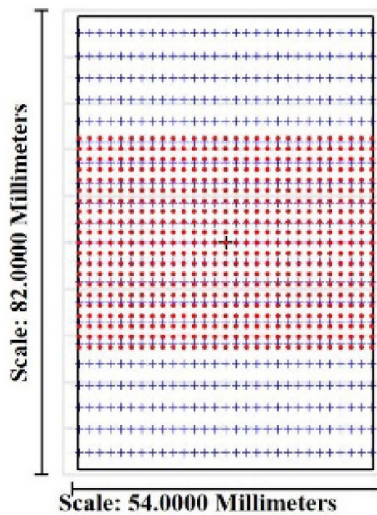**Figure 11.** Results obtained after the elimination of the misalignment aberration from figure 10.

Figure 12. Footprints of rays on the imaging plane (blue) and those on the test surface (red).

$\times$ 18.5 mm $= 0.0058\lambda$ PV, where L is the central thickness of the partial null. Therefore, the glass homogeneity error can be neglected.

For wedge errors in the plane-convex lens, simulations are conducted to investigate its contributions to test result. Figure 15 shows the influence when the wedge errors is 23″. It shows that to limit the test error within 0.01λ RMS, the wedge error of the partial null should be smaller than $\pm23''$.
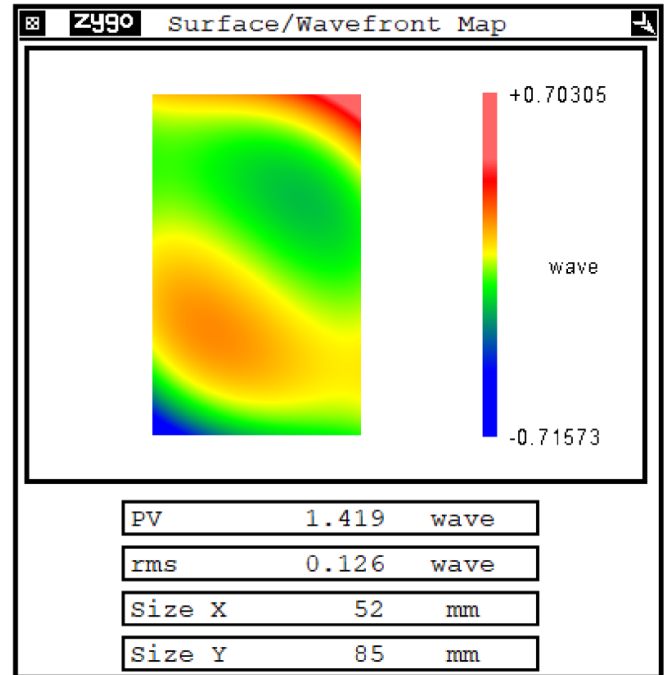

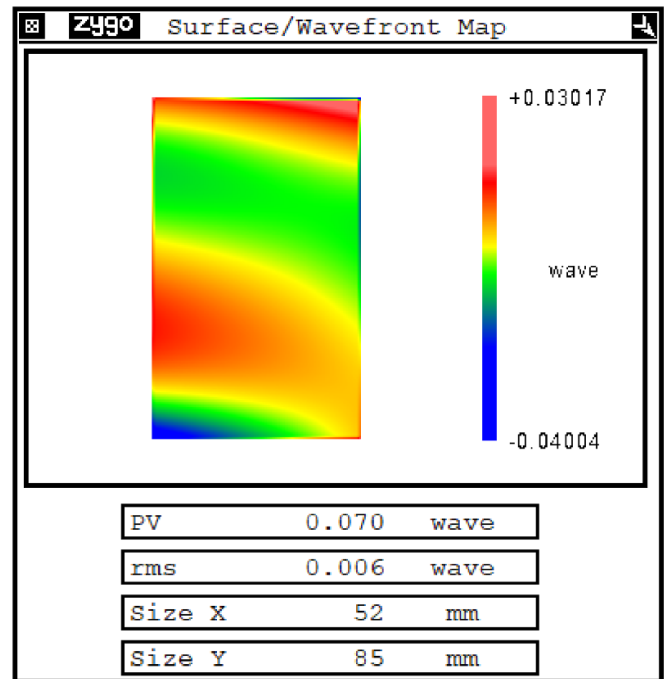**Figure 13.** Plot of the recovered surface after phase and mapping corrections.

Figure 14. Point-to-point difference between the recovered and the theoretical surfaces figures.

Retrace error correction accuracy is determined by the modeling accuracy of the test system. The modeling error includes inaccurate modeling of the partial null and the test surface, which include the inaccurate element structure parameters and element position inconsistences with the actual system. The influence of surface figure error of the cylindrical

9

Table 2. Misalignment aberration for testing aspheric cylinders.

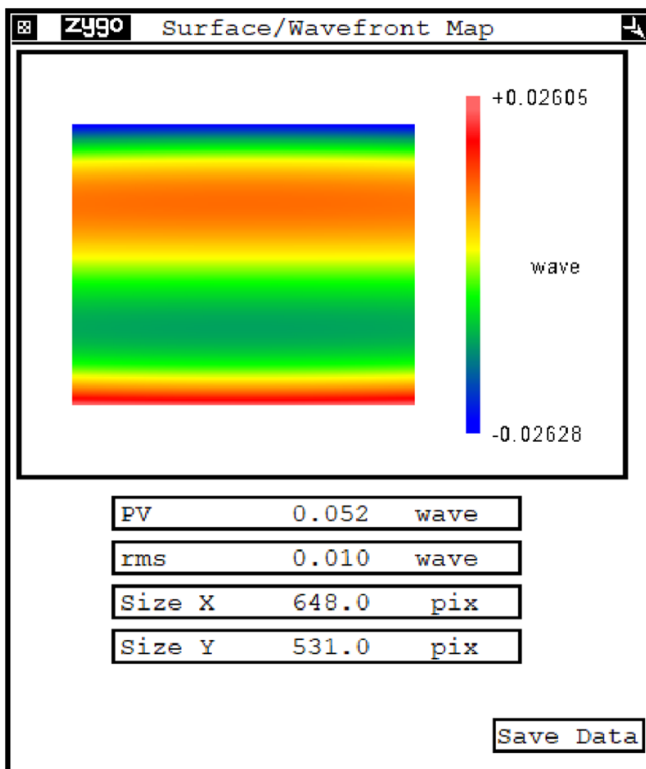| Misalignment	Interferogram	Misalignment aberration	Aberration type
t_x			Tilt-*y*
t_y			Tilt-*x*
t_z			Twist
d_y			Tilt-*y*
d_z			Power-*y*

Figure 15. Influence of wedge errors in the partial null.

surface of the partial null, the surface figure error of the flat surface of the partial null, and the wedge error of the partial null on the test result is 0.015λ RMS, 0.004λ RMS, and 0.01λ RMS, respectively. As for the position modeling error,

their contribution is about 0.01λ RMS as analyzed above. To sum up, the total modeling error influence is about $\lambda/50$ RMS. Modeling error is the dominant error source of the method. The contributions of other error sources such as reference error and noise error are weak. Therefore, measuring accuracy of the method is about $\lambda/50$ RMS.

3. Results

To verify the feasibility of the proposed method, an aspheric cylinder with $k = -1$ and $R = 200$ mm was measured with the use of the proposed method. The clear aperture of the test method was $D_a \times D_l = 85 \times 52$ mm^2 (arc direction $\times$ linear direction). The parameters of the partial null were $r_1 = 54.274$ mm, $D_{an} \times D_{ln} = 52 \times 52$ mm^2 (arc direction $\times$ linear direction), BK7 glass material, and center thickness $T = 18.5$ mm. Notably, the parameters of the test surface and partial null are the same as those in the principal part. The test system was designed as shown in figure 3. The distance from the flat surface of the near-null to the test surface was 293.032 mm. A near-null test system was established, as shown in figure 16. The interferometer was a Zygo GPI 4" with a transmissive flat (TF). The near-null test result was obtained with a PV 5.951λ and an RMS 1.011λ, as shown in figure 17. After phase and mapping corrections, the surface figure was recovered, as shown in figure 18, with a PV of 3.053λ and an RMS of 0.677λ.

For the cross-test, the surface was tested using the stigmatic null test method with a high-accuracy retro-flat. The test system was designed as shown in figure 19. Tracing one ray (the ray marked in red in figure 19) emitted from the interferometer can help explain the principle of operation of the test
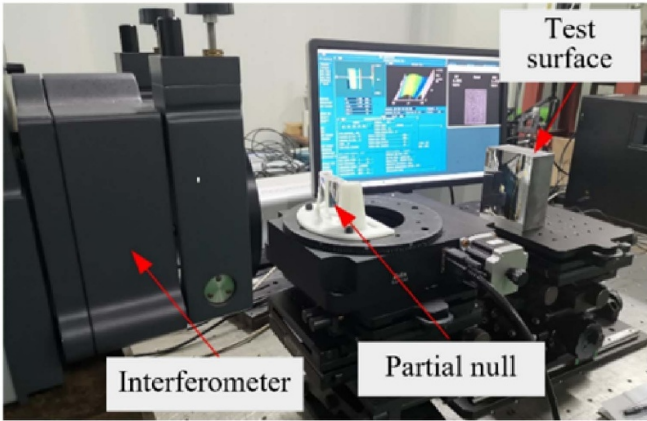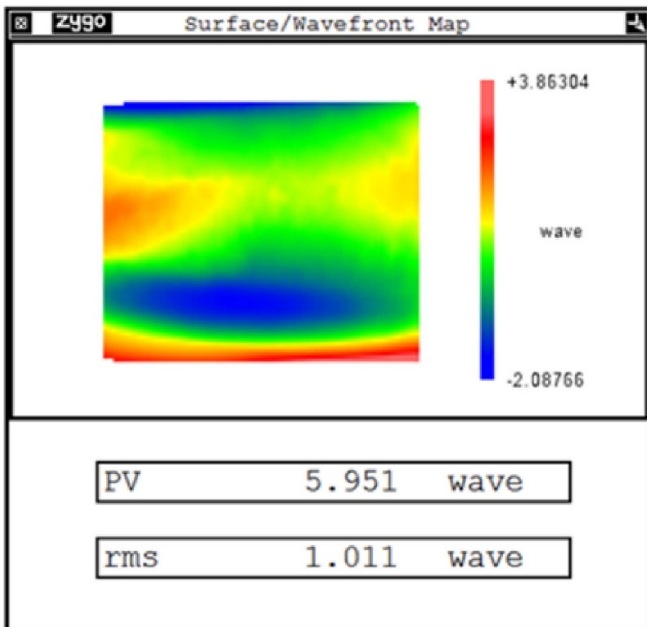
Figure 16. Experimental layout.

Figure 17. Near-null test result.

Figure 18. Recovered surface figure.

system. The collimated beam, which is emitted from the interferometer with a standard TF, hits the test surface. The reflected beam converges to the focus line of the test surface. The focus distance of the aspheric cylinder was $R/2 = 100$ mm. The reference surface of the TF was located at the focus line. The normal direction of the TF was the same as the normal direction of the center of the test surface. Hence, the beam was reflected at the TF and hit the test surface. The beam was converted to a collimated beam after it was reflected at the test surface, and was transmitted back to the interferometer to interfere with the reference beam in the interferometer. Notably, the collimated beam that was transmitted back to the interferometer was flipped about the *y*-axis compared with the emergent beam from the interferometer. The experimental layout is illustrated in figure 20. The test results of the stigmatic null test are shown in figure 21 with a PV of 2.486λ and an RMS of 0.526λ. In the test result, the component of the surface figure
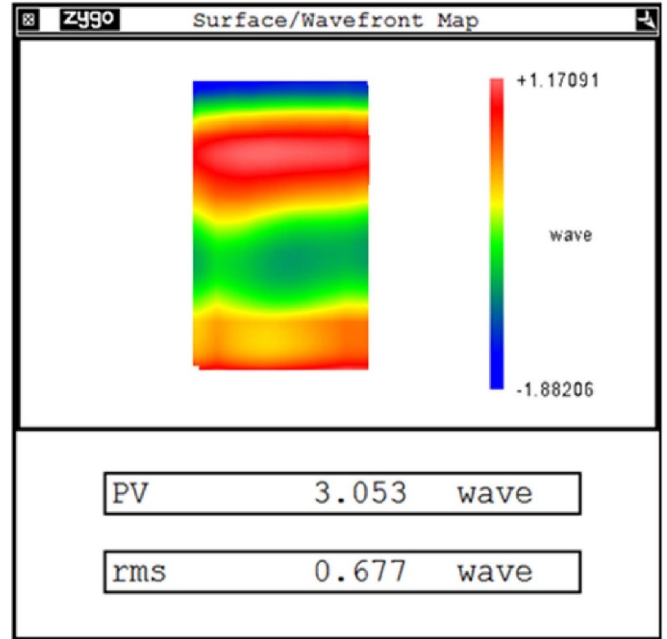
that is symmetric along the *y*-axis is doubled, and the component of the surface figure that is antisymmetric along the *y*-axis is eliminated. The test data of the near-null test are added to the component that is flipped about the *y*-axis to compare them with those of the stigmatic null test. The reconstructed test data of the near-null test are shown in figure 22 with a PV of 2.903λ and an RMS of 0.577λ.

The RMS difference of the results shown in figures 21 and 22 is about $\lambda/20$. Furthermore, to quantitatively evaluate the similarity of error distribution of the two results, SSIM index [37] proposed for image quality assessment was introduced to compare the two test results. The SSIM index is defined as

$$S_k(m,n) = \frac{(2\mu_m\mu_n + C_1)(2\sigma_{mn} + C_2)}{(\mu_m{}^2 + \mu_n{}^2 + C_1)(\sigma_m{}^2 + \sigma_n{}^2 + C_2)}, \quad (22)$$

where μ_m and μ_n are the grayscale means of two images, respectively, and σ_m and σ_n are the grayscale standard deviations of the two images, respectively. The constant $C_1 = (K_1 L)^2$, $C_2 = (K_2 L)^2$,, $K_1 \ll 1$, $K_2 \ll 1$, set the values of $K_1 = 0.01$ and $K_2 = 0.03$. L is the grayscale range for the 8-bit grayscale image, such that $L = 255$. The index was equal to one for two identical images. The SSIM index of the two test results was $S = 0.906$. This indicates that the similarity between the surface figure distribution of the two results is relatively high. Thus, the test accuracy of the proposed near-null test method was verified.

4. Discussion

Compared with the state-of-the-art flexible null test methods for testing aspheric cylinders, that is, the yawing CGH method [30], the proposed method is proven to have merits regarding the coaxial design of the test system. The alignment of the
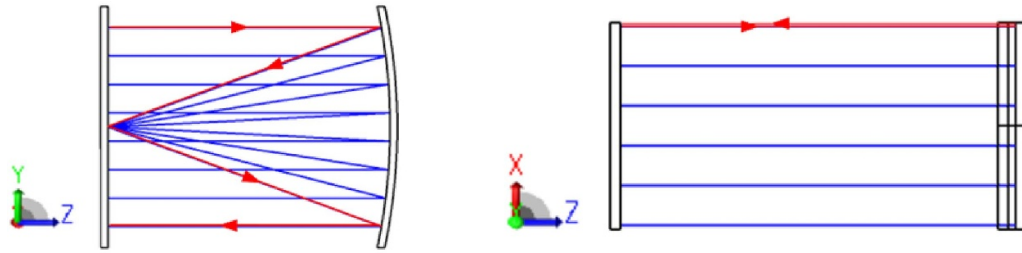
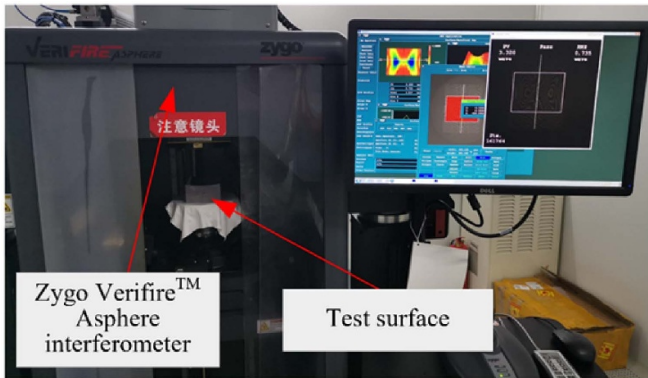**Figure 19.** Test system of the stigmatic null test. (a) Front and (b) top views.

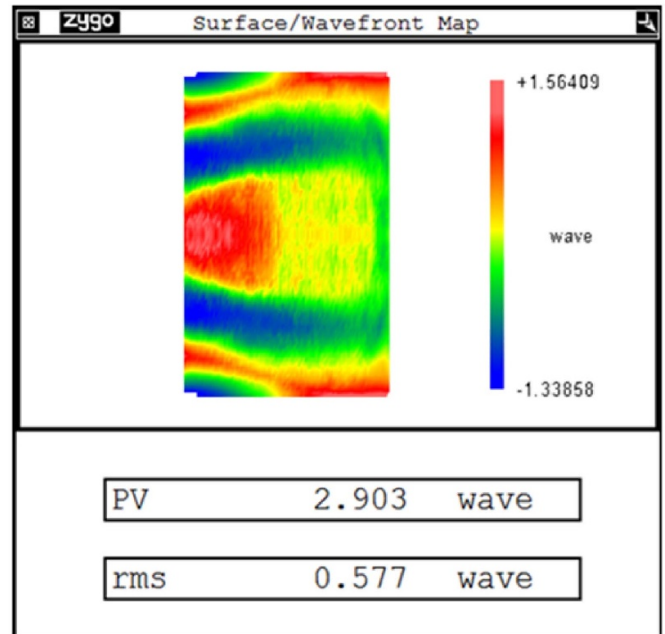**Figure 20.** Experimental layout of the stigmatic null test.

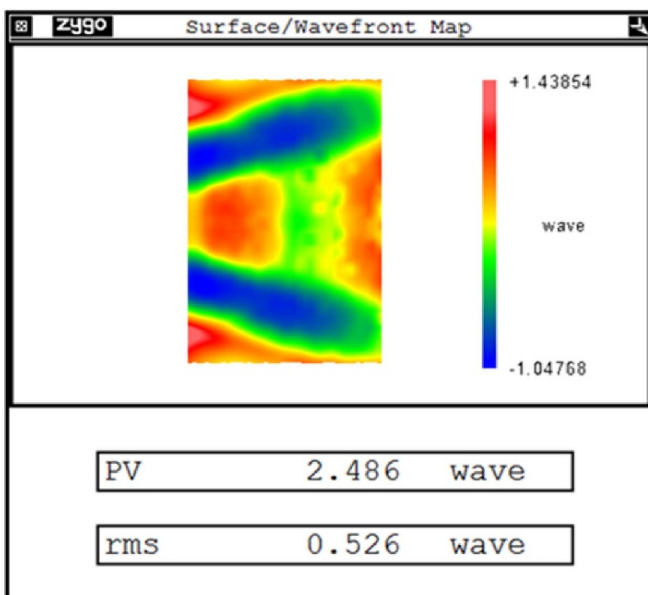**Figure 22.** Reconstructed test data of the near-null test.

Figure 21. Test result of the stigmatic null test.

test surface and null was much easier. Furthermore, only one translational motion was required to test various aspheric cylinders. The translation motion was easier to conduct, and the motion accuracy could be controlled by low-coherence interferometry within ± 1 μm. In contrast, it is difficult to guarantee the yaw accuracy in the flexible null-test method by yawing the CGH. The proposed method can obtain a full aperture surface figure error map using one shot. In contrast, stitching is

required to obtain the full aperture figure error in the flexible null-test method by yawing the CGH, which further complexes the test system and decreases the test accuracy. Moreover, the proposed method was used to investigate the partial null theory for aspheric cylinders and the relationship between the partial null parameters and testable surface parameters. The test ability of a certain partial null was clearly identified, which has not been reported in previous methods. The testable aspheric cylinders were equidistant surfaces with constant shape parameters $k \cdot R$. These were determined by the shape parameters of the partial null lens, that is, based on the solution of the equation $kR = -Pf$. The investigation in partial null theory and testability analysis provides an efficient aspheric cylinder design guide for engineers, who typically construct prototypes of high-energy laser systems to design a series of aspheric cylinders that can be conveniently and rapidly tested by a certain partial null. It can also help metrologists design a single partial null or a series of partial nulls for testing various aspheric cylinders. Therefore, the proposed method can serve as a reference for engineers who want to use aspheric cylinders in high-energy laser systems. We believe that this will further

promote the application of aspheric cylinders in high-energy laser systems.

The proposed method, however, has a few drawbacks; for example, only aspheric cylinders with a nearly constant kR value can be tested by a certain partial null. The measurable range is relatively narrow. However, additional work, such as the design of a series of nulls, can mitigate this issue. Prospects for further development of the proposed method are described as follows.

(a) One partial null has very limited flexibility. Once the null optic has been chosen, there is basically no flexibility apart from the trivial ones: The selection of the position of the surface under test (which is more or less determined by the Roc of the surface under test) and the non-null testing capability of the basic interferometer. In that sense, the advantage of the method compared to state of the art (CGH) is the better availability of the null optic and the disadvantage is that the compensation is not complete. The partial null was reported herein as a positive cylindrical lens for testing concave parabolic aspheric cylinders and near parabolic aspheric cylinders. For aspheric cylinders with oblate cross-sections, a negative cylindrical lens can be designed following the processes described in section 2. To overcome the limited measurement range of the proposed method, a series of partial nulls can be designed to cover the common $k \cdot R$ range of aspheric cylinders in certain applications. This will further improve the flexibility and measurement efficiency of the aspheric cylinders.

(b) Another method can efficiently broaden the measurement range of the proposed method instead of using a series of partial nulls. A CGH can be inserted between the TF and cylindrical lens to transform the flat wavefront to a convergent cylindrical wavefront. The cylindrical lens was located between the focus line of the CGH and the test surface. By moving the cylindrical lens back and forth relative to the focus line and varying the distance from the test surface to the cylindrical lens, a much wider range of aspheric cylinders can be tested in the near-null test condition. Various aspheric cylinders with different $k \cdot R$ values can be tested without changing the cylindrical null lens. By optimizing the parameters of the cylindrical null lens, different equidistant surface groups with considerable variations in the $k \cdot R$ values can be tested. The method was verified by testing aspheric surfaces [38]. The application of the method for testing aspheric cylinders is currently under investigation. We hope to report our findings on this matter in the future

(c) Commonly, the residual aberrations existing in near-null tests are within the phase modulation range/strokes of the adaptive optics (AO) elements. Introducing AO elements, such as spatial light modulators and deformative mirrors, to null the residual aberration of the proposed method will further turn the near null test to a null test. The retrace error of near-null tests can be eliminated. Furthermore, the AO elements can enhance the testability of the proposed method. Near aspheric cylinders, such as free

forms having a base with the shape of an aspheric cylinder, can be tested. Moreover, in-process aspheric cylinders with unknown severe local surface figure errors beyond the dynamic range of commercial interferometers can be tested. This is possible if we use an optimization algorithm to control the AO elements to iteratively generate adaptive nulls until the interferogram fringes can be resolved. This adaptive null method for testing aspheric surfaces and free-form surfaces with base shapes of aspheric surfaces has already been investigated [39–52]. However, to the best of our knowledge, the application of the adaptive null method for testing aspheric cylinders or free-form surfaces with base shapes of aspheric cylinders has never been reported previously. This method is currently being researched

5. Conclusions

The proposed method successfully advances the flexible null test for aspheric cylinders from the stitching to the one-shot mode, from off-axis and complex configurations to coaxial and simple configurations. The simple configuration and the developed near-null data processing method guarantee the test accuracy of $\sim\lambda/20$ RMS. The theoretical analysis shows the testable aspheric cylinders are equidistant surfaces have a nearly constant shape parameter $k \cdot R$. A practical near-null test system was developed. Its flexible test capacity, simple configuration, and test accuracy were successfully validated by testing a concave aspheric cylinder with $R = 200$ mm, $k = -1$ and an aperture of 85×52 mm^2. The proposed method can help enhance the test efficiency for aspheric cylinders. The test accuracy verification and testability analyses can serve as a reference for engineers who intend to use aspheric cylinders in high-energy laser systems, and promote the application of aspheric cylinders in high-energy laser systems. However, our method also has a few drawbacks; for example, a partial null can only adapt surfaces with a constant shape parameter $k \cdot R$, which is a very narrow test range. Serial partial null, which enlarges the test range, requires further studies.

Conflict of interest

The authors declare no conflicts of interest.

Author contributions

Shuai Xue: Conceptualization, Methodology, Software, Visualization, Investigation, Writing- Original draft preparation. Lingwei Kong: Data curation. Yifan Dai: Supervision. Shanyong Chen: Writing- Reviewing and Editing. Zhifan Lin: Writing- Reviewing and Editing.

ORCID iD

Shuai Xue ⬤ https://orcid.org/0000-0002-7390-2326

References

[1] Hodgson N and Weber H 2005 *Laser Resonators and Beam Propagation: Fundamentals, Advanced Concepts and Applications* (Berlin: Springer)

[2] Lü B, Xu S, Hu Y and Cai B 1992 Matrix representation of three-dimensional astigmatic resonators *Opt. Quantum Electron.* **24** 619–30

[3] Gu D, Liu W and Zhou Q 2013 The research of wavefront compensation of a reflective beam shaping system *Proc. SPIE* **8904** 890415

[4] Huang P, Wu X, To S, Zhu L and Zhu Z 2020 Deterioration of form accuracy induced by servo dynamics errors and real-time compensation for slow tool servo diamond turning of complex-shaped optics *Int. J. Mach. Tool Manuf.* **154** 103556

[5] Kordonsky W, Prokhorov I, Gorodkin G, Jacobs S, Puchebner B and Pietrowski D 1993 Magnetorheological finishing *Opt. Photon. News* **4** 16–17

[6] Wyant J and MacGovern A 1970 Computer generated holograms for testing aspheric optical elements *Int. Symp. Appl. de I'Holographie* pp 13–18

[7] Dresel T, Schwider J, Wehrhahn A and Babin S 1995 Grazing incidence interferometry applied to the measurement of cylindrical surfaces *Opt. Eng.* **34** 3531–5

[8] Peng J, Xu H, Yu Y and Chen M 2015 Stitching interferometry for cylindrical optics with large angular aperture *Meas. Sci. Technol.* **26** 025204

[9] Peng J, Wang Q, Peng X and Yu Y 2015 Stitching interferometry of high numerical aperture cylindrical optics without using a fringe-nulling routine *J. Opt. Soc. Am.* A **32** 1964–72

[10] Peng J, Chen D and Yu Y 2017 Stitching interferometry of a full cylinder without using overlap areas *Meas. Sci. Technol.* **28** 085001

[11] Chen D, Peng J, Valyukh S, Asundi A and Yu Y 2018 Measurement of high numerical aperture cylindrical surface with iterative stitching algorithm *Appl. Sci.* **8** 2092

[12] Chen D, Wang C, Valyukh S, Wu X and Yu Y 2020 Bayesian uncertainty evaluation of stitching interferometry for cylindrical surface *Measurement* **157** 107626

[13] Reardon P, Liu F and Geary J 2010 Schmidt-like corrector plate for cylindrical optics *Opt. Eng.* **49** 053002

[14] Xue S, Dai Y, Zeng S, Chen S, Tian Y and Shi F 2021 Interferometric stitching method for testing cylindrical surfaces with large apertures *Opt. Express* **29** 19767–89

[15] Peng J, Chen D, Guo H, Zhong J and Yu Y 2018 Variable optical null based on a yawing CGH for measuring steep a cylindrical surfaces *Opt. Express* **16** 20306–18

[16] Liu H, Hao Q, Zhu Q and Sha D 2004 Testing an aspheric surface using part-compensating lens *Trans. Beijing Inst. Technol.* **24** 625–8

[17] Hao Q, Li T, Hu Y, Wang S, Ning Y, Tan Y and Zhang X 2017 Vertex radius of curvature error measurement of aspheric surface based on slope asphericity in partial compensation interferometry *Opt. Express* **25** 18107–21

[18] Liu D, Yang Y, Tian C, Luo Y and Wang L 2009 Practical methods for retrace error correction in nonnull aspheric testing *Opt. Express* **17** 7025–35

[19] Liu D, Shi T, Zhang L, Yang Y, Chong S and Shen Y 2014 Reverse optimization reconstruction of aspheric figure error in a non-null interferometer *Appl. Opt.* **53** 5538–46

[20] Greivenkamp J and Gappinger R 2004 Design of a non-null interferometer for aspheric wavefronts *Appl. Opt.* **43** 5143–51

[21] Gappinger R and Greivenkamp J 2004 Iterative reverse optimization procedure for calibration of aspheric wave-front measurements on a nonnull interferometer *Appl. Opt.* **43** 5152–61

[22] Tian C, Yang Y and Zhuo Y 2012 Generalized data reduction approach for aspheric testing in a non-null interferometer *Appl. Opt.* **51** 1598–604

[23] Zhang L, Liu D, Shi T, Yang Y and Shen Y 2013 Practical and accurate method for aspheric misalignment aberrations calibration in non-null interferometric testing *Appl. Opt.* **52** 8501–11

[24] He Y, Hou X, Quan H and Song W 2015 Retrace error reconstruction based on point characteristic function *Opt. Express* **23** 28216–23

[25] Shi T, Liu D, Zhou Y, Yan T, Yang Y, Zhang L, Bai J, She Y, Miao L and Huang W 2017 Practical retrace error correction in non-null aspheric testing: a comparison *Opt. Commun.* **383** 378–85

[26] Malacara D 2007 *Optical Shop Testing* (New York: Wiley)

[27] Dall H 1947 A null test for paraboloids *J. Br. Astron. Assoc.* **57** 201–5

[28] Wu F 1997 Design of compensator for null test of aspherical surface interferometer *J. Appl. Opt.* **18** 10–13

[29] Mahajan V 2010 Orthonormal aberration polynomials for anamorphic optical imaging systems with rectangular pupils *Appl. Opt.* **49** 6924–9

[30] Peng J, Ge D, Yu Y, Wang K and Chen M 2013 Method of misalignment aberrations removal in null test of cylindrical surface *Appl. Opt.* **52** 7311–23

[31] Peng J, Yu Y and Xu H 2014 Compensation of high-order misalignment aberrations in cylindrical interferometry *Appl. Opt.* **53** 4947–56

[32] Zeng X, Zhang X, Xue D, Zhang Z and Jiao J 2018 Mapping distortion correction in freeform mirror testing by computer-generated hologram *Appl. Opt.* **57** F56–61

[33] Novak M, Zhao C and Burge J 2008 Distortion mapping correction in aspheric null testing *Proc. SPIE* **7063** 706313

[34] Zemax Corp., Zemax OpticsStudio 20.2 User Manual

[35] Noll R 1976 Zernike polynomials and atmospheric turbulence *J. Opt. Soc. Am.* **66** 207–11

[36] Xue S, Chen S, Shi F and Lu J 2016 Sub-aperture stitching test of a cylindrical mirror with large aperture *Proc. SPIE* **9684** 96840C

[37] Wang Z, Bovik A, Sheikh H and Simoncelli E 2004 Image quality assessment: from error visibility to structural similarity *IEEE Trans. Image Process.* **13** 600–12

[38] Xue S, Chen S and Tie G 2018 Near-null interferometry using an aspheric null lens generating a broad range of variable spherical aberration for flexible test of aspheres *Opt. Express* **26** 31172–89

[39] Pruss C and Tiziani H 2004 Dynamic null lens for aspheric testing using a membrane mirror *Opt. Commun.* **233** 15–19

[40] Fuerschbach K, Thompson K and Rolland J 2014 Interferometric measurement of a concave, φ-polynomial, Zernike mirror *Opt. Lett.* **39** 18–21

[41] Zhang L, Zhou S, Li D, Li J and Yu B 2018 Model-based adaptive non-null interferometry for freeform surface metrology *Chin. Opt. Lett.* **16** 081203

[42] Zhang L, Zhou S, Li D, Liu Y, He T, Yu B and Li J 2018 Pure adaptive interferometer for free form surfaces metrology *Opt. Express* **26** 7888–98

[43] Zhang L, Zhou S, Li J and Yu B 2019 Deep neural network based calibration for freeform surface misalignments in general interferometer *Opt. Express* **27** 33709–23

[44] Zhang L, Li C, Xiao Huang Y, Zhang S Z, Li J and Yu B 2020 Compact adaptive interferometer for unknown freeform surfaces with large departure *Opt. Express* **28** 1897–912

[45] Huang L, Choi H, Zhao W, Graves L and Kim D 2016 Adaptive interferometric null testing for unknown freeform optics metrology *Opt. Lett.* **41** 5539–42

[46] Kacperski J and Kujawinska M 2006 Active, LCoS based laser interferometer for microelements studies *Opt. Express* **14** 9664–78

[47] Cashmore M, Hall S and Love G 2014 Traceable interferometry using binary reconfigurable holograms *Appl. Opt.* **53** 5353–8

[48] He Y, Huang L, Hou X, Fan W and Liang R 2017 Modeling near-null testing method of a freeform surface with a deformable mirror compensator *Appl. Opt.* **56** 9132–8

[49] Cao Z, Xuan L, Hu L, Liu Y, Mu Q and Li D 2005 Investigation of optical testing with a phase-only liquid crystal spatial light modulator *Opt. Express* **13** 1059–65

[50] Xue S, Chen S, Fan Z and Zhai D 2018 Adaptive wavefront interferometry for unknown free-form surfaces *Opt. Express* **26** 21910–28

[51] Xue S, Chen S, Tie G and Tian Y 2019 Adaptive null interferometric test using spatial light modulator for free-form surfaces *Opt. Express* **27** 8414–28

[52] Xue S, Chen S, Tie G, Tian Y, Hu H, Shi F, Peng X and Xiao X 2019 Flexible interferometric null testing for concave free-form surfaces using a hybrid refractive and diffractive variable null *Opt. Lett.* **44** 2294–7